A Porosity Method to Describe Complex 3D-Structures Theory and Application to an Explosion

M.-F. Robbe

A theoretical method was developed to be able to describe the influence of structures of complex shape on a transient fluid flow without meshing the structures. Structures are considered as solid pores inside the fluid and act as an obstacle for the flow. The method was specifically adapted to fast transient cases.
The porosity method was applied to the simulation of a Hypothetical Core Disruptive Accident in a small-scale replica of a Liquid Metal Fast Breeder Reactor. A 2D-axisymmetrical simulation of the MARS test was performed with the EUROPLEXUS code. Whereas the central internal structures of the mock-up could be described with a classical shell model, the influence of the 3D peripheral structures was taken into account with the porosity method.

Keywords: porosity method, homogenization, nuclear reactor, explosion, fluid-structure coupling.

1 Introduction

In case of a Hypothetical Core Disruptive Accident (CDA) in a Liquid Metal Fast Breeder Reactor, the contact between fuel and liquid sodium creates a high-pressure gas bubble in the core. The violent expansion of this bubble loads and deforms the vessel and the internal structures.

During the 1970s and 1980s, large programmes of investigations devoted to the understanding of CDA were undertaken. They included both experimental tests in small-scale mock-ups, and simulations with specialized computer codes to extrapolate the experimental results to the reactor size and to check the LMFBR integrity.

Based on a 1/30-scale model of the Superphenix reactor, the MARA programme [1, 2] was performed at CEA-Cadarache. It involved ten tests of gradual complexity due to the addition of internal deformable structures:

- MARA 1 and 2 considered a vessel partially filled with water and closed by a rigid roof [3].
- MARA 4 represented, in addition, the main core support structures [4].
- MARA 8 and 9 were closed by a flexible vessel and a flexible roof [5].
- MARA 10 included the core support structures and a simplified representation of the structures above the core [6].

To end this series of tests, the MARS test [7] was a 1/20-scale mock-up including all the significant internal components.

At the end of the 1980s, a specific CDA sodium-bubble-argon tri-component constitutive law [8] was developed in the general ALE fast dynamics finite element CASTEM-PLEXUS code. This first version of the CDA constitutive law was validated [9] with the CONT benchmark [10].

In order to demonstrate the CASTEM-PLEXUS capability to predict the behaviour of real reactors [11, 12], axisymmetrical computations of the MARA series were confronted with the experimental results. The computations performed at the beginning of the 1990s showed a rather good agreement between the experimental and computed results for the MARA 8 and MARA 10 tests, even if there were some discrepancies [13]. On the contrary, the prediction of the MARS structure displacements and strains was overestimated [14].

In 1999, the CASTEM-PLEXUS code was merged with the PLEXIS-3C code [15] (a former joint product by CEA and JRC) to extend the capacities of both codes. The new-born EUROPLEXUS code benefitted from a new method to deal with the fluid-structure coupling.

New simulations were undertaken with the new coupling, and compared with the experimental results for:

- The MARA 8 mock-up [16, 17].
- The MARA 10 mock-up [18, 19].
- The MARS mock-up with a finer mesh, and without the representation of the non-axisymmetrical structures [20]. Even if the results of the MARS test were better, the deformation of some structures was still overestimated, since the finer mesh introduced an additional flexibility.

The conservatism was supposed to come from the very simple representation of the MARS non-axisymmetrical structures (core elements, pumps and heat exchangers) by a pressure loss. These structures, acting as porous barriers, should have a protective effect on the containment by absorbing energy and slowing down the fluid impacting the containment.

Therefore, a new CDA constitutive law taking into account the presence of the internal structures (without meshing them) by means of an equivalent porosity method [21] was developed. Another simulation with the porous model was carried out to estimate the influence of the latter structures [22].

This paper presents a brief description of the porosity model, the MARS mock-up and the analysis of the results computed by the EUROPLEXUS code with the porous model. The main central structures are described with a classical shell model, while the heat exchangers and pumps are described with the porous model.

2 Porosity model

The purpose is to define a method able to represent the influence of structures located inside a fluid pool, during a fast transient fluid flow, without meshing them. The idea is based on the substitution of an equivalent "porous" fluid for the structures and the surrounding fluid. Structures are assimilated to a set of solid marbles regularly distributed into the fluid.

Globally, the method consists in averaging the behaviour of the fluid surrounding structures on the volume filled by fluid and structures. The method is divided into three steps:

- The fluid conservation laws are space-averaged on the control volume to consider the partial occupation of the control volume by fluid. The fluid equations are written with fluid, solid and control volume terms. As we consider that a solid is rigid, it is pointless studying the solid conservation laws.
- The fluid equations are modified, by introducing a porosity coefficient, in order to replace the control volume terms by fluid ones. Except a fluid-solid force, the fluid conservation laws just depend on fluid variables.
- An equivalent "porous" fluid, with its own properties, is finally defined on the control volume. The conservation laws of this medium are matched up with the fluid equations previously defined.

The main hypotheses are:

- The fluid is considered homogeneous, even if it is composed of a mixture of several fluids.
- Thermal transfers and phase changes are considered as negligible, as thermal exchanges are much slower than acoustic transients.
- Structures are assumed to be rigid and no fluid-structure coupling is considered. The model only simulates the structure presence as an obstacle for the fluid flow. Neither the recoil and deformation of structures is described, nor the energy absorbed during their deformation.
- No mass source and no heat source are included in the theoretical model. However, both terms are easy to add in the conservation equations.

An Eulerian approach was used in order to eliminate the temporal variations of the control volume. This simplification allows to have fixed boundaries for all the spatial integrals concerning the control volume. An extension of the present method to the ALE description (Arbitrary Lagrange Euler) should be possible by taking into consideration variations of the spatial boundaries versus time.

The local conservation laws of a fluid are:

$$\text{mass } \frac{\partial}{\partial t}\rho_f + div(\rho_f \vec{v}_f) = 0$$

$$\text{momentum } \frac{\partial}{\partial t}(\rho_f \vec{v}_f) + d\vec{i}v(\rho_f \vec{v}_f \otimes \vec{v}_f) - d\vec{i}v\,\overline{\overline{\sigma_f}} - \rho_f \vec{g} = \vec{0}$$

$$\text{total energy } \frac{\partial}{\partial t}\left[\rho_f\left(u_f + \frac{1}{2}\vec{v}_f \cdot \vec{v}_f\right)\right] + div\left[\rho_f\left(u_f + \frac{1}{2}\vec{v}_f \cdot \vec{v}_f\right)\vec{v}_f\right]$$
$$-div(\overline{\overline{\sigma_f}} \cdot \vec{v}_f) - \rho_f \vec{g} \cdot \vec{v}_f = 0,$$

where the subscript f is relative to fluid variables, t indicates time, ρ the density, v the velocity, σ stresses, g the gravity, and u the internal energy.

2.1 Average on the control volume

Let us consider a fixed control volume or total volume Ω_t cut by an interface A_s (Fig. 1). This interface divides the control volume into a fluid subvolume Ω_f and a solid subvolume Ω_s. Let us note A_t the surface bounding jointly the fluid volume and the control volume.

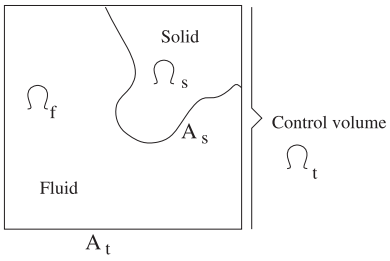

Fig. 1: Control volume

Let $\Theta(x, y, z, t)$ be a function (scalar, vector or tensor) defined on the control volume Ω_t. $\overline{\Theta}(x, y, z, t)$ is the average value of Θ on the control volume Ω_t.

$$\overline{\Theta} = \frac{1}{\Omega_t}\int_{\Omega_f} \Theta \, d\Omega .$$

The fluid conservation laws averaged on the control volume become:

Mass

$$\frac{\partial}{\partial t}(\overline{\rho_f}) + div(\overline{\rho_f \vec{v}_f}) = 0$$

Momentum

$$\frac{\partial}{\partial t}(\overline{\rho_f \vec{v}_f}) + d\vec{i}v(\overline{\rho_f \vec{v}_f \otimes \vec{v}_f}) - d\vec{i}v\,\overline{\overline{\sigma_f}} - \overline{\rho_f \vec{g}}$$
$$-\frac{1}{\Omega_t}\oint_{A_s} \vec{n}_f \cdot \overline{\overline{\sigma_f}}\, dA = \vec{0}$$

Total energy

$$\frac{\partial}{\partial t}\left[\overline{\rho_f\left(u_f + \frac{1}{2}\vec{v}_f \cdot \vec{v}_f\right)}\right] + div\left[\overline{\rho_f\left(u_f + \frac{1}{2}\vec{v}_f \cdot \vec{v}_f\right)\vec{v}_f}\right]$$
$$-div\left(\overline{\overline{\sigma_f} \cdot \vec{v}_f}\right) - \overline{\rho_f \vec{g} \cdot \vec{v}_f} - \frac{1}{\Omega_t}\oint_{A_s} \vec{n}_f \cdot \left(\overline{\overline{\sigma_f}} \cdot \vec{v}_f\right) dA = 0.$$

2.2 Average on the fluid volume

Let us consider that $\underline{\Theta}(x, y, z, t)$ is the average value of Θ on the fluid volume Ω_f.

$$\underline{\Theta} = \frac{1}{\Omega_f}\int_{\Omega_f} \Theta \, d\Omega .$$

Let β be the porosity, defined as the fluid presence fraction inside the control volume: $\beta = \Omega_f / \Omega_t$. The average values $\overline{\Theta}$ and $\underline{\Theta}$ are linked by: $\overline{\Theta} = \beta\underline{\Theta}$.

The mass equation can be transformed easily into:

$$\beta\frac{\partial}{\partial t}\underline{\rho_f} + div\,(\beta\,\underline{\rho_f}\,\underline{\vec{v}_f}) = 0.$$

The same method applied to the momentum equation introduces new terms:

$$\beta\frac{\partial}{\partial t}(\underline{\rho_f}\,\underline{\vec{v}_f}) + d\vec{i}v(\beta\underline{\rho_f}\,\underline{\vec{v}_f}\otimes\underline{\vec{v}_f}) + d\vec{i}v\left(\beta\underline{\rho_f}\,\underline{\vec{v}_f'\otimes\vec{v}_f'}\right) - d\vec{i}v\left(\beta\underline{\overline{\overline{\sigma_f}}}\right) - \beta\underline{\rho_f}\,\vec{g} - \frac{1}{\Omega_t}\oint_{A_s}\vec{n}_f\cdot\underline{\overline{\overline{\sigma_f}}}\,\mathrm{d}A = \vec{0}$$

The terms with ' correspond to fluctuating terms. If we consider a function ϕ, defined on the fluid volume Ω_f, it can be separated into a fluid average term $\underline{\phi}$ and a fluctuating term ϕ' (white noise):

$$\phi = \underline{\phi} + \phi'.$$

The stress tensor $\underline{\overline{\overline{\sigma_f}}}$ can be split into a pressure tensor including the diagonal terms and a viscous-stress tensor containing the non-diagonal terms:

$$\underline{\overline{\overline{\sigma_f}}} = \underbrace{-\underline{p_f}\,\overline{\overline{I}}}_{\text{pressure}} \underbrace{-\frac{2}{3}\mu(div\,\underline{\vec{v}_f})\,\overline{\overline{I}} + \mu\left(\underline{\overline{\overline{grad}}\,\vec{v}_f} + {}^{t}\underline{\overline{\overline{grad}}\,\vec{v}_f}\right)}_{\text{viscous stresses}}$$

where p is pressure, $\overline{\overline{I}}$ the unit tensor, and μ the dynamic viscosity.

The term $-\underline{\rho_f}\,\underline{\vec{v}_f'\otimes\vec{v}_f'}$ is analogous to Reynolds stresses (turbulent stresses) and can also be separated into a pressure tensor and a viscous-stress tensor:

$$-\underline{\rho_f}\,\underline{\vec{v}_f'\otimes\vec{v}_f'} = \underline{\overline{\overline{\sigma_{\mathrm{Re}}}}} = \underbrace{-\frac{2}{3}\underline{\rho_f}\,k_T\,\overline{\overline{I}}}_{\text{similar to a pressure}} \underbrace{-\frac{2}{3}\mu_T(div\,\underline{\vec{v}_f})\,\overline{\overline{I}} + \mu_T\left(\underline{\overline{\overline{grad}}\,\vec{v}_f} + {}^{t}\underline{\overline{\overline{grad}}\,\vec{v}_f}\right)}_{\text{similar to viscous stresses}},$$

where k_T is the turbulent kinetic energy and μ_T the turbulent viscosity.

After having eliminated the negligible terms, the global stress tensor becomes:

$$\underline{\overline{\overline{\sigma_f}}} + \underline{\overline{\overline{\sigma_{\mathrm{Re}}}}} = -\underline{p_f}\,\overline{\overline{I}} - \frac{2}{3}\mu_T(div\,\underline{\vec{v}_f})\,\overline{\overline{I}} + \mu_T\left(\underline{\overline{\overline{grad}}\,\vec{v}_f} + {}^{t}\underline{\overline{\overline{grad}}\,\vec{v}_f}\right)$$

.

The integral on the solid surface can be written versus basic variables:

$$-\frac{1}{\Omega_t}\oint_{A_s}\vec{n}_f\cdot\underline{\overline{\overline{\sigma_f}}}\,\mathrm{d}A = \underline{p_f}\left(\frac{1}{\Omega_t}\oint_{A_s}\vec{n}_f\,\mathrm{d}A\right) - \frac{1}{\Omega_t}\oint_{A_s}\vec{n}_f\cdot\left(-p_f'\,\overline{\overline{I}} + \underline{\overline{\overline{\tau_f}}}\right)\mathrm{d}A = -\underline{p_f}\,grad\,\beta - \beta\,\vec{F}_s,$$

where $\beta\,\vec{F}_s$ is the solid-fluid interaction force and contains all the stress terms different from the one in average pressure.

According to [23] and supposing an approximate symmetry of structures, the tri-dimensional interaction force can be written with the following expression:

$$-\beta\,\vec{F}_s = \beta\frac{1}{2}\left(\frac{A_s}{\Omega_t}\,{}^{t}\vec{\xi}\,\overline{\overline{I}}\right)\cdot\underline{\rho_f}\left|\underline{\vec{v}_f}\right|\underline{\vec{v}_f},$$

where $\vec{\xi}$ contains the coefficients of pressure loss.

Thus we can deduce the final expression of the momentum conservation law:

$$\beta\frac{\partial}{\partial t}(\underline{\rho_f}\,\underline{\vec{v}_f}) + d\vec{i}v(\beta\underline{\rho_f}\,\underline{\vec{v}_f}\otimes\underline{\vec{v}_f}) + \beta\,grad\,\underline{p_f} - d\vec{i}v\left[-\frac{2}{3}\beta\mu_T(div\,\underline{\vec{v}_f})\,\overline{\overline{I}} + \beta\mu_T\left(\underline{\overline{\overline{grad}}\,\vec{v}_f} + {}^{t}\underline{\overline{\overline{grad}}\,\vec{v}_f}\right)\right] - \beta\,\underline{\rho_f}\,\vec{g} + \beta\frac{1}{2}\frac{A_s}{\Omega_t}\,{}^{t}\vec{\xi}\,\overline{\overline{I}}\cdot\underline{\rho_f}\left|\underline{\vec{v}_f}\right|\underline{\vec{v}_f} = \vec{0}.$$

Finally, the total energy equation can be rewritten:

$$\beta\frac{\partial}{\partial t}\left[\underline{\rho_f}\left(\underline{u_f} + \frac{1}{2}\underline{\vec{v}_f}\cdot\underline{\vec{v}_f}\right)\right] + div\left[\beta\underline{\rho_f}\left(\underline{u_f} + \frac{1}{2}\underline{\vec{v}_f}\cdot\underline{\vec{v}_f}\right)\underline{\vec{v}_f}\right] + div\left[\beta\,\underline{p_f}\,\underline{\vec{v}_f}\right] - div\left[\left(-\frac{2}{3}(div\,\underline{\vec{v}_f})\,\overline{\overline{I}} + \underline{\overline{\overline{grad}}\,\vec{v}_f} + {}^{t}\underline{\overline{\overline{grad}}\,\vec{v}_f}\right)\cdot\beta\,\mu_T\,\underline{\vec{v}_f}\right] - \beta\,\underline{\rho_f}\,\underline{\vec{v}_f}\cdot\underline{\vec{g}} = 0.$$

2.3 Definition of a "porous" fluid equivalent to the averaged medium

The initial problem was formulated with conservation laws defined on the control volume, subdivided into a fluid zone and a solid zone, and using variables of both components. Then the conservation laws were averaged on the fluid; this process allowed to have only fluid equations defined on the fluid subvolume and with fluid variables. To return to the ini-

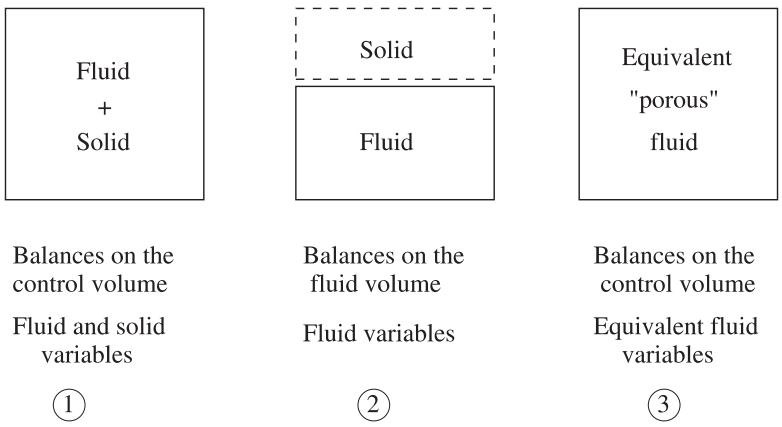

Fig. 2: Steps of the "porosity" method

tial control volume, it is necessary to consider an equivalent fluid defined on the control volume and whose properties have to be determined (Fig. 2).

The equivalent "porous" fluid can be considered as a single substance filling the entire control volume. It is governed by the classical conservation laws with an additional force term in the momentum equation:

mass

$$\frac{\partial}{\partial t}\rho_{eq} + div\,(\rho_{eq}\,\vec{v}_{eq}) = 0,$$

momentum

$$\frac{\partial}{\partial t}(\rho_{eq}\,\vec{v}_{eq}) + \vec{div}\,(\rho_{eq}\,\vec{v}_{eq}\otimes\vec{v}_{eq}) + grad\,p_{eq}$$
$$-\vec{div}\left[-\frac{2}{3}\mu_{T_{eq}}(div\,\vec{v}_{eq})\bar{\bar{I}} + \mu_{T_{eq}}\left(\overline{\overline{grad}}\,\vec{v}_{eq} + {}^{t}\overline{\overline{grad}}\,\vec{v}_{eq}\right)\right]$$
$$-\rho_{eq}\,\vec{g} + \vec{F}_{eq} = \vec{0},$$

total energy

$$\frac{\partial}{\partial t}\left[\rho_{eq}\left(u_{eq} + \frac{1}{2}\vec{v}_{eq}\cdot\vec{v}_{eq}\right)\right] + div\left[\rho_{eq}\left(u_{eq} + \frac{1}{2}\vec{v}_{eq}\cdot\vec{v}_{eq}\right)\vec{v}_{eq}\right]$$
$$+ div\,(p_{eq}\,\vec{v}_{eq})$$
$$-div\left[\left(-\frac{2}{3}(div\,\vec{v}_{eq})\bar{\bar{I}} + \overline{\overline{grad}}\,\vec{v}_{eq} + {}^{t}\overline{\overline{grad}}\,\vec{v}_{eq}\right)\cdot\mu_{T_{eq}}\,\vec{v}_{eq}\right]$$
$$-\rho_{eq}\,\vec{g}\cdot\vec{v}_{eq} = 0.$$

Comparing term by term these equations with the fluid conservation laws averaged on the fluid volume, we obtain the value of each equivalent variable:

$$\rho_{eq} = \beta\,\underline{\rho_f} \qquad \vec{v}_{eq} = \underline{\vec{v}_f} \qquad p_{eq} = \beta\,\underline{p_f}$$
$$u_{eq} = \underline{u_f} \qquad \mu_{T_{eq}} = \beta\,\mu_T$$
$$\vec{F}_{eq} = -\underline{p_f}\,grad\,\beta + \beta\frac{1}{2}\frac{A_s}{\Omega_t}\,{}^{t}\vec{\xi}\,\bar{\bar{I}}\cdot\underline{\rho_f}\left|\underline{\vec{v}_f}\right|\underline{\vec{v}_f}\,.$$

Compared with classical fluid conservation laws, the solid presence introduces three new parameters: a porosity β describing the volumic filling rate of structures into the fluid medium, a pressure loss coefficient $\vec{\xi}$ induced by the fluid-solid friction and a coefficient A_s/Ω_t describing the global structure shape.

In addition to the fact that the new equations (mass, momentum and total energy) are written with equivalent variables, the momentum equation contains two new forces: a fluid-solid interaction force $\beta\,\vec{F}_s$ and a force $\underline{p_f}\,grad\,\beta$ at the interface between two equivalent media presenting different porosities.

3 Description of the MARS mock-up

The primary circuit of the Superphenix reactor (Fig. 3) is enclosed in the main reactor vessel [24]. This vessel is welded to the roof slab, and encased in a safety vessel. Both vessels are made of stainless steel.

The MARS experiment (Fig. 4) (1 m in diameter and 1 m high) includes all the significant internal components of the reactor [7]. The main vessel is an assembly of a cylindrical part made of 316L stainless steel, and a torospherical bottom

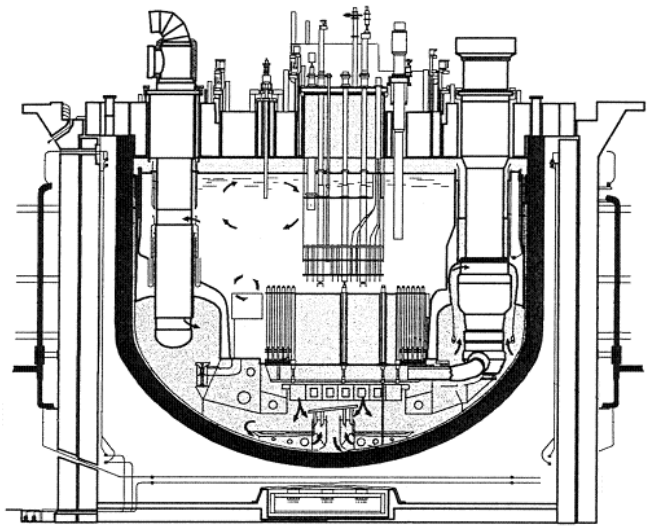

Fig. 3: The Superphenix reactor

made of 304L stainless steel. Its thickness varies between 0.8 and 1.6 mm.

The unmelted part of the core is simulated by aluminum cylinders and steel hexagons fixed into two AG3 aluminum plates. The neutron shielding is represented by four radial shells and the associated supporting structures. The mock-up also includes the strongback, the diagrid support, two inner vessels, the anti-convecting device, the core catcher and the main vessel cooling system.

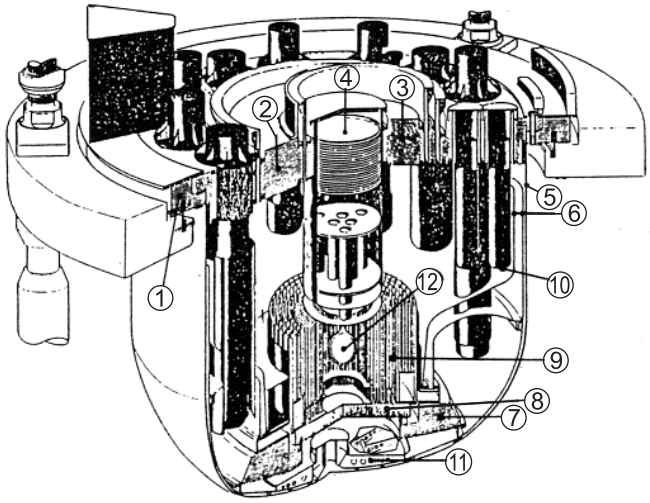

① – roof
② – large rotating plug
③ – small rotating plug
④ – core cover plug
⑤ – main vessel
⑥ – internal vessels
⑦ – core support structures
⑧ – diagrid support
⑨ – core and neutron shieldings
⑩ – pumps and heat exchangers
⑪ – core catcher
⑫ – gas bubble in the middle of the core

Fig. 4: The MARS mock-up

The roof slab is constituted by two circular plates of different thicknesses. Openings are drilled to enable the passage of the large components. The two rotating plugs are concentrically off as in the reactor. The core cover plug was simplified compared to the reactor one: however, it includes a top plate, a heat-insulation, spacer plates, an in-pile shell and pipes.

The main components inserted through the roof slab (4 primary pumps, 8 intermediate heat exchangers, 4 emergency cooling exchangers, 2 integrated purification devices), as well as the supporting and joining rings are present. Rubber-ring bands simulate the heat-insulating material between the roof and the main vessel. Other components above the top closure are represented by their inertia using lead plates.

The thin structures are mainly made of 304L stainless steel in order to simulate the austenistic steel of the reactor structures. The massive structures and those made of heterogeneous materials (roof slab, rotating plugs, core support structure, diagrid support) are made of A5 aluminum. The top plate of the core cover plug is made of A42 aluminum.

The sodium coolant at operating conditions is simulated by water at 20 °C. The cover gas of the mock-up is the same as in the reactor (argon). The test was fired using an 80 g low-density low-pressure explosive charge of L54/16 composition [25]. The charge mass was chosen to simulate the 800 MJ full-scale mechanical energy release used in the reference CDA in the Superphenix reactor. The explosive charge was supported by the base of the core cover plug.

The test was well instrumented with: pressure transducers, accelerometers, strain gauges, high-speed cameras, and a grid drawn on the different structures.

4 Numerical modelling of the mock-up

4.1 The EUROPLEXUS code

EUROPLEXUS [26, 27, 28] is a general finite element code, co-developed by CEA-Saclay and JRC-Ispra, and devoted to the analysis of fast transient phenomena. It results from the merging of the CASTEM-PLEXUS and PLEXIS-3C codes, and can perform 1D, 2D or 3D fluid-structure calculations as required. A commercial version of the code for industrial use is available through the Samtech software house.

The main fields dealt with are impacts [29], explosions [30, 31, 32], pipe circuits [33, 34, 35], blowdowns [36, 37, 38, 39], hydrodynamics [40] and articulated systems [41].

EUROPLEXUS is mainly based on the Finite Element Method, but it also contains finite volumes and spectral elements. Time integration is explicit and realised with a Newmark algorithm. The formulation can be Lagrangian, Eulerian or Arbitrary Lagrange Euler (ALE). The code can take into account various non-linearities related to materials or geometry.

4.2 Geometry

Owing to the symmetry of the MARS mock-up, a 2D-axisymmetrical representation was chosen. The external structures are modeled by shells or massive elements. The main internal structures are represented with a classical shell model. The peripheral components are described with the porosity model homogenizing the components with the surrounding fluid.

The main vessel is modelled with a thin shell, and two materials for the cylindrical and torospherical parts. The vessel is supposed rigidly fixed to the roof. The mock-up is hung to the rigid frame by a cylindrical shell.

The top closure is assimilated to an axisymmetrical structure composed of massive elements. The openings for the passage of the components are simply accounted for by the mass they remove to the roof. Local masses are added above the top closure to consider the mass of the instrumentation, the lead plates, and the peripheral components. The core cover plug was simplified: the heat and neutronic insulation is simulated by three plates, and the pipes are assimilated to two cylinders.

The rings joining the roof slab and the three plugs are represented with thin aluminum shells at the top, and rubber shells at the base of the massive structures. The heat-insulating material between the roof and the main vessel is represented by a rubber-ring band.

In the centre of the mock-up, a single rigid structure (called Core Support Structures) describes the strongback, the neutron shielding support, the support of the baffles and the internal vessel as they are fitted together. The CSS is assimilated to an axisymmetrical rigid shell of constant thickness, and whose mass is the total mass of all the structures. The CSS is attached to the vessel by a cylindrical collar.

The diagrid support is described by a thin shell, connected to the CSS by a swivel link. The core is schematized by an added mass distributed along the diagrid. The neutron shielding is modelled by its central shell since it governs the fluid port between the core cover plug and the shielding, and a local mass added at the base of the first shell to take into account the three other shells.

The baffles surrounding the neutron shielding are assimilated to a vertical axisymmetrical shell. Only the central shell of the internal vessel is meshed; the other is described by a local mass. The shielding, the baffle, and the internal vessel are embedded in the CSS. The core catcher is represented by a mass distributed along the base of the main vessel.

4.3 Materials

The behaviour of the structures is generally described with isotropic elasto-plastic constitutive laws. However elastic laws are used for the rubber elements of weak resistance joining the roof and the plugs. The cylinders schematizing the pipes of the core cover plug are described by an elastic law approximated by the homogenization of the non-axisymmetrical structures. The behaviour of the core support structure is supposed to be linear elastic.

The 3D geometry of the peripheral components (pumps, heat exchangers, purification devices) cannot be meshed correctly with an axisymmetrical model. So their presence is accounted for thanks to the porosity model: the fluid elements comprised between the extreme radii of the peripheral components are homogenized with the structures.

The peripheral structures are described by a volume filling rate of 47 %. Even if the model allows to take into account a pressure loss by friction, this possibility is not used in this

simulation. Figs. 5 and 6 present the global mesh and that of the structures. The porous zone corresponds to the trapezoidal area between the internal vessel and the roof.

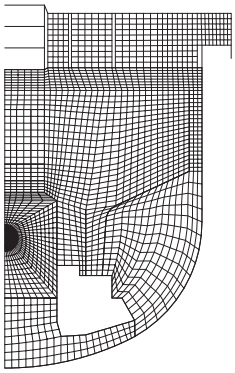

Fig. 5: Mesh of the MARS test

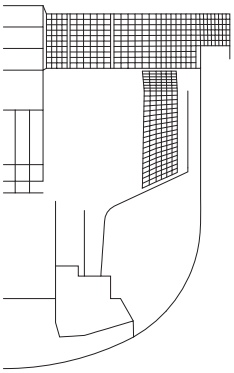

Fig. 6: Mesh of structures

The CDA constitutive law is used to describe all the fluid filling the mock-up. This law is devoted to tri-component fluid mixtures, for which one of the components can be diphasic. In the mock-up, the fluids intervening are water, argon and the explosive charge.

Argon is supposed to be a perfect gas with an adiabatic behaviour.

$$p_a^{(n+1)} = p_a^{(n)} \left(\frac{p_a^{(n+1)}}{p_a^{(n)}} \right)^{\lambda_a},$$

where the initial density is $\rho_a^{(0)} = 1.658$ kg/m^3, and the heat capacity ratio is $\lambda_a = c_p / c_v = 1.67$. Argon is initially at atmospheric pressure $p_a^{(0)} = 10^5$ Pa.

The explosive charge (bubble) is described by a perfect gas with a polytropic law.

$$p_b^{(n+1)} = p_b^{(n)} \left(\frac{p_b^{(n+1)}}{p_b^{(n)}} \right)^{\eta_b},$$

where the initial density is $\rho_b^{(0)} = 400$ kg/m^3, the initial pressure is $\rho_b^{(0)} = 2.88\ 10^8$ Pa, and the polytropic coefficient $\eta_b = 1.322$.

Water is described by a perfect and isothermal fluid.

$$p_w^{(n+1)} = p_g^{(n+1)} = p_w^{(n)} + C_w^2 (\rho_w^{(n+1)} - \rho_w^{(n)})$$

with an initial density $\rho_w^{(0)} = 998.3$ kg/m^3, a sound velocity $C_w = 1550$ m/s. Water is initially at atmospheric pressure $p_w^{(0)} = 10^5$ Pa.

The pressure of the gas mixture p_g is the sum of the partial pressures of the gases:

$$p_g^{(n+1)} = p_a^{(n+1)} + p_b^{(n+1)} + p_v^{(n+1)}.$$

Water is supposed to be at saturation conditions. However if $p_w^{(n+1)} > p_{sat}$, the presence fraction of the vapour is negligible. If the pressure decreases, water can reach saturation pressure, and the vaporisation is supposed to be instantaneous. The vapour is an isothermal perfect gas whose pressure is constant and only depends on the initial temperature $T^{(0)}$:

$$p_v^{(n+1)} = p_{\text{saturation}}(T^{(0)}).$$

4.4 Fluid-structure coupling

Structures are represented with a Lagrangian description. The bubble zone is kept fixed and is Eulerian. Water and argon are described with an Arbitrary-Lagrange-Euler modelling, apart from the homogenized zone. The porosity model implemented in EUROPLEXUS is available only for the Eulerian description, so that the homogenized zone must be Eulerian. Two element layers next to the internal vessel are left out of the homogenized zone to operate the fluid-structure coupling.

The fluid-structure coupling implemented in EUROPLEXUS works without coupling elements; the code automatically writes the relations between the fluid and solid nodes facing each other.

In the core cover plug, no fluid-structure coupling is defined:

- Between the internal cylinders and the fluid as the fluid can cross the pipes simulated by vertical cylinders.
- At the top of the external cylinder surrounding the plug because this shell is perforated in the mock-up.

In order to preserve a regular mesh inside the core cover plug, the fluid nodes along the three cylinders have to stay aligned between the structure nodes at the connections with the plates.

5 Analysis of the Results of the Simulation

In the following part of the paper, we will call:

- Central zone: the area limited by the in-pile shell of the CCP, the neutron shielding and the diagrid.
- Free opening: the free space between the top of the neutron shielding and the edge of the in-pile shell of the CCP.
- Bottom zone: the area limited by the diagrid, the CSS and the bottom of the main vessel.
- Intermediate zone: the area between the neutron shielding and the lower part of the internal vessel.
- Lateral zone: the area on the right side between the internal vessel, the CSS and the torospherical part of the main vessel.
- Channel: the space between the upper part of the internal vessel and the cylindrical part of the main vessel.
- Upper zone: the area below the top closure.

5.1 Pressure

Fig. 7 presents the pressure versus time. Initially, water and argon are at atmospheric pressure whereas the explosive charge simulating the gas bubble is at 288 MPa. From 0.02 ms, a pressure wave issued from the bubble zone expands spherically.

The pressure wave hits successively:

- The central structures at 0.06 ms.

Fig. 7: Pressure

- The baffle and the CCP from 0.1 ms.
- The internal vessel from 0.18 ms.
- The bottom of the main vessel at 0.22 ms.
- The upper part of the main and the internal vessels between 0.34 and 0.4 ms.

From 0.1 to 0.22 ms, the diagrid and the Core Support Structure (CSS) hold back the propagation of the pressure wave, so that pressure increases up to 160 MPa in the bottom right-hand corner of the central zone, while it remains lower than 60 MPa below the diagrid. The expansion of the pressure wave causes a pressure decrease in the centre of the bubble and at the bottom of the CCP.

The pressure wave keeps a spherical shape until 0.22 ms. Then the vertical progression is limited by the presence of the main vessel at the bottom and the argon layer at the top. So the wave progresses laterally and crashes progressively against the main vessel. At 0.38 ms, the wave forms a sort of queue that impacts the top of both vessels.

At 0.26 ms, the pressure is maximum below the diagrid (25 MPa) and in the intermediate zone (18 MPa). The pressure decreases down to atmospheric pressure at the bottom of the central and intermediate zones, and at the top of the CCP. The pressure always remains low in the argon layer owing to the gas compressibility.

From 0.42 to 1 ms, the pressure globally diminishes, and even reaches 12 MPa in some areas. Between 1.2 and 2.6 ms, the pressure globally becomes lower than 5 MPa. The pressurised area along the rounded corner slides up to the channel. The overpressure around the central zone moves towards the peripheral components and the top of the CCP.

The top of the CCP remains pressurised until 3.7 ms due to the convergence of the upward water flows in the CCP, and the horizontal flows coming from the top closure. Until 4.7 ms, the pressurised area slides horizontally below the roof towards the top right-hand corner.

Between 5 and 6 ms, the rebound of water against the CSS pressurises the lateral zone. Afterwards, the pressure becomes lower than 5 MPa in the entire mock-up.

Two main differences appear compared with the computation without the massive peripheral structures:

When the pressure wave crashes against the vessels at about 0.34 ms, the passing of the wave is slightly delayed and the maximum pressure is higher (20 MPa on the front face of the porous zone, instead of 17 MPa in the corner joining the intermediate and upper parts of the internal vessel).

The overpressure in the upper zone between 2.8 and 3.5 ms remains lower than 3 MPa and slides upwards along the porous zone, instead of reaching 11 MPa and impacting directly the upper part of the internal vessel.

5.2 Gas fraction

Figs. 8 to 10 show the general volume presence fraction of the gas, the mass presence fractions of the bubble and the argon, respectively. Initially, the mock-up is filled with water, except the explosive charge in the centre and the argon layer below the top closure.

The gas bubble grows spherically until 0.2 ms. Then it expands preferentially upwards and takes a rectangular shape, homothetic to that of the central area at 0.8 ms. The bubble deviates towards the free opening, and starts escaping in the upper zone from 1.6 ms.

Water remains trapped at the bottom of the central area due to the expansion of the bubble and the confinement of the central structures. From 0.4 ms, water vaporises in the areas which become depressurised after the passing of the pressure wave.

The bubble escapes from the central zone until 7 ms, creating a large panache of pressurised gas in the upper zone. The pressurisation induced by the panache condenses steam in the upper and intermediate zones at 5 ms. Nevertheless, the steam layers along the internal vessel and the diagrid still exist until 6 and 8 ms, respectively.

The pressure wave impacting the top closure starts compressing the argon layer upwards at 0.2 ms. From 1.6 to 4 ms, the panache propels water upwards, which in turn pushes and compresses the low-pressure argon gas into the top right-hand corner of the mock-up. From 5 to 17 ms, the argon bag is pushed down in the channel by the violent water flows below the top closure.

From 8 ms, the expansion of the bubble gas out of the central area is stopped by the rebound of water against the top closure and the internal vessel. The front of the panache flows sideways and a whirlpool forms; the base of the panache becomes thinner. Due to the general depressurisation from 6 ms on, the argon expands back along the top closure.

The whirlpool pushes back the bubble gas in the central area from 13 ms. At 17 ms, the bubble almost completely fills the central area. The panache goes slightly away from the free opening and forms a torus that twirls round in the middle of the water.

Some gas flows down along the outer side of the neutron shielding and remains trapped between the shielding and the baffle. The argon gathers and forms a bag at the top of the CCP. As fluid flows back from the channel over the internal vessel, a second bag of argon forms near the top right-hand corner.

After 30 ms, the central area is completely diphasic. Water vaporises along the main vessel bottom and the diagrid due to the depressurisation of the bottom zone.

The main difference when the computation is done without the peripheral structures concerns steaming. Larger amounts of vapour appear in the porous zone and for a longer time between 1.2 and 3 ms. It seems that the panache extends a bit less in the new simulation.

5.3 Fluid velocity

Figs. 11 and 12 show the fluid orientation and the fluid velocities. The fluid is initially at rest in the whole mock-up. From 0.02 ms, the bubble expands spherically with a velocity of 200 m/s.

At 0.1 ms, the high speed on the symmetry axis comes from the horizontal blocking condition. The confinement of the central area induces a speed decrease in the lower part. The central structures are hit at 0.1 ms.

The pressure wave accelerates the water at the periphery of the central zone: water impacts successively between 0.12 and 0.3 ms the baffle, the bottom of the internal vessel, all the spacer plates of the CCP, and the vessel bottom. The

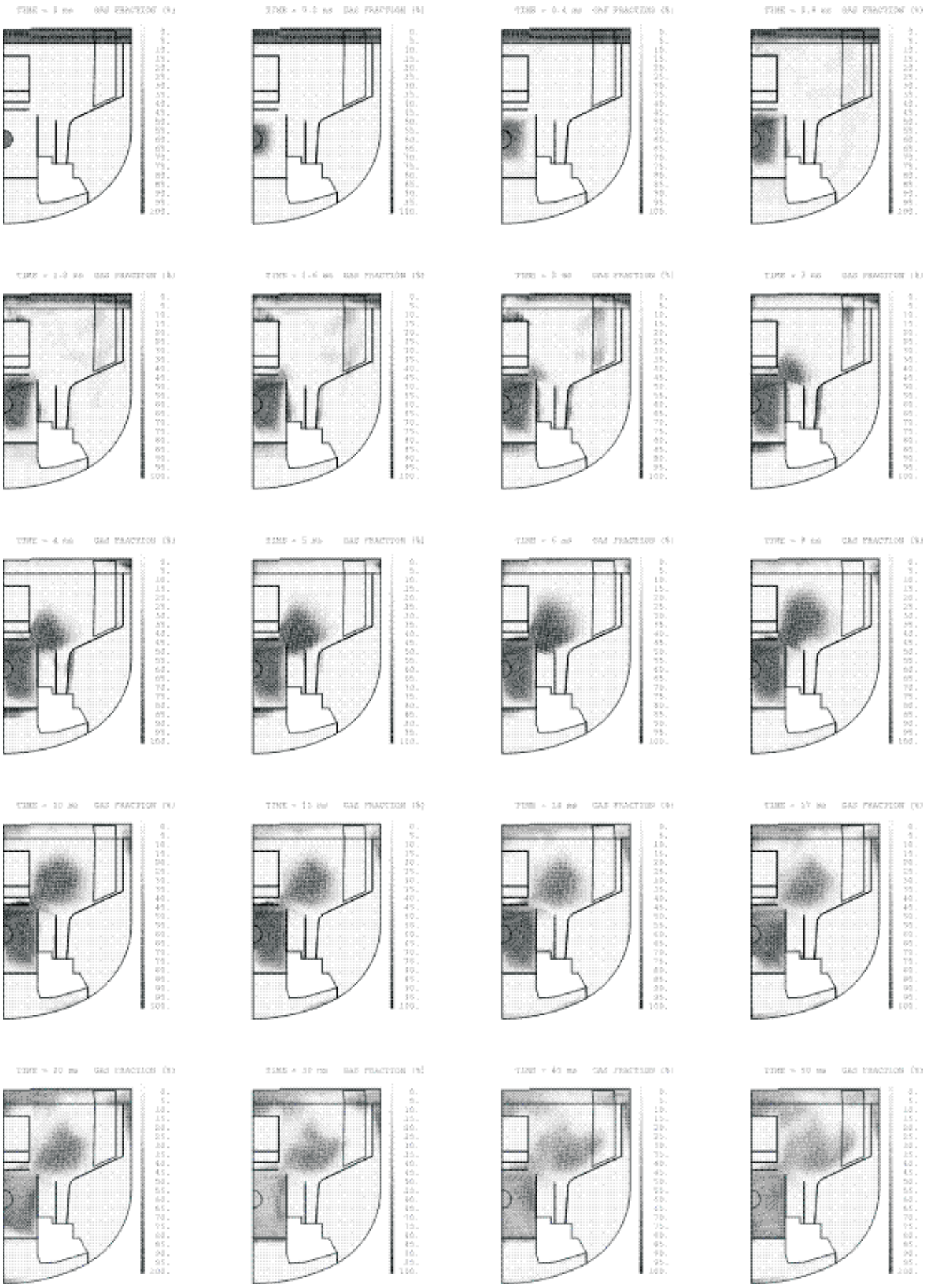

Fig. 8: Volume presence fraction of gas

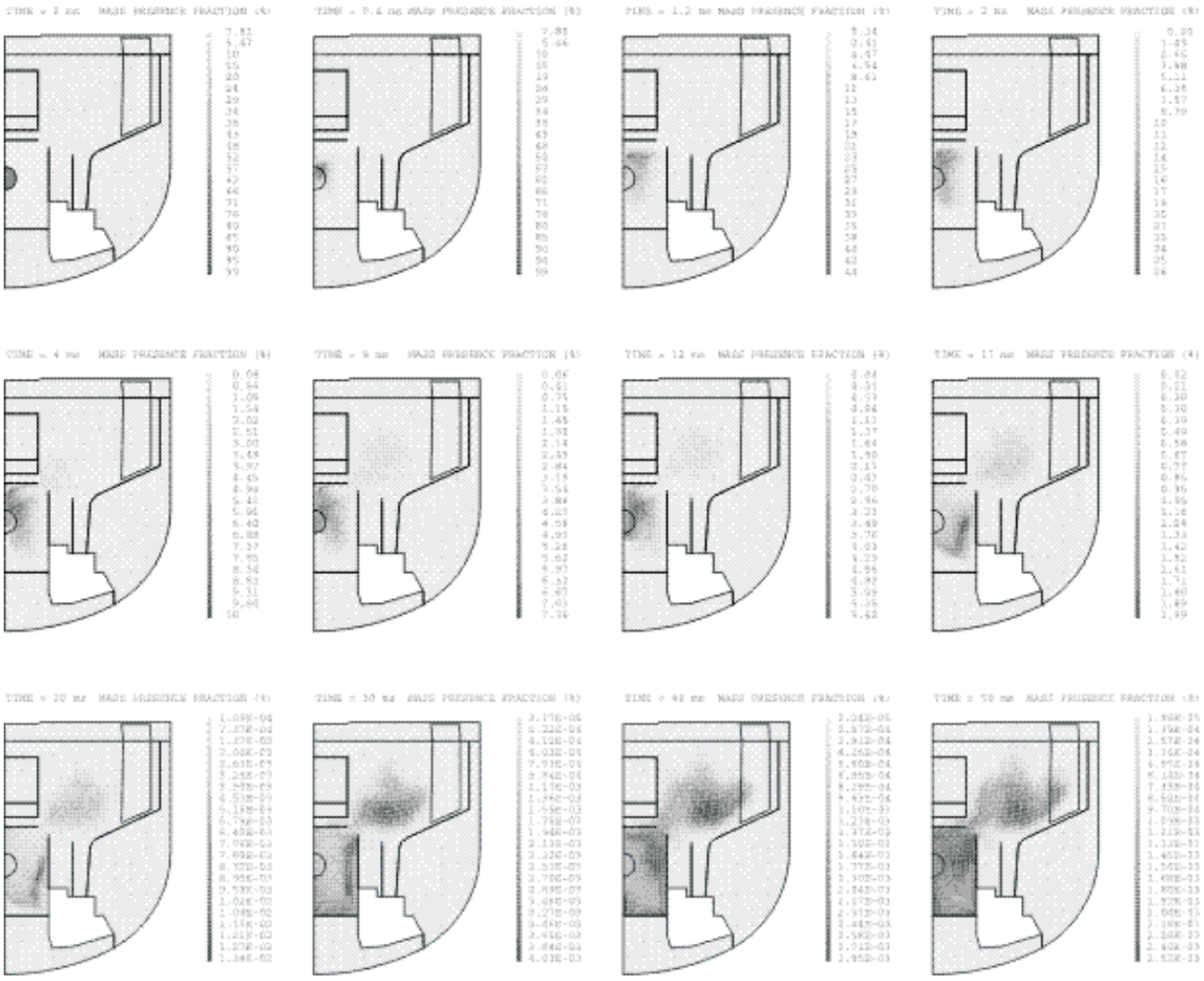

Fig. 9: Mass presence fraction of the bubble

speed falls to 140 m/s in the free opening, and water impacts the neutron shielding at 80 m/s.

Between 0.38 and 0.8 ms, the bubble flows towards the free opening at 100 m/s. The water progressively hits all the external structures: the highest speeds reach 30 m/s at the bottom of the main vessel and 40 m/s in the heat-insulation of the CCP. The argon leaves the top of the CCP horizontally by the perforated part of the external cylinder.

From 1 to 2.4 ms, the bubble crosses the free channel with velocities up to 90 m/s, and directly impacts the top of the neutron shielding. Out of the central area, the water flows:

- Down towards the bottom of the main vessel and the collar.
- Laterally towards the rounded corner and the channel.
- Upwards and diagonally towards the upper part of the internal vessel.

The upward water flows below the top closure expel the argon out of the CCP, and horizontally towards the top right-hand corner.

From 3 to 5 ms, the bubble flows out of the central area violently and forms a gas panache. The panache pushes water down between the neutron shielding and the baffle, upwards and diagonally towards the top right-hand corner. The thin argon layer slides outwards along the top closure at 80 m/s. Water bounces back against the CSS and flows back toward the internal vessel. In the bottom zone, the water flow reverses.

Until 7 ms, the panache progresses in the upper zone at a speed up to 90 m/s, and sucks up the water of the intermediate zone. The water in the CCP slows down and deviates inwards near the top. In the channel, the convergence of the upward water flows from the lateral zone and the downward argon flows from the top corner, and leads to an outward horizontal thrust.

The progression of the panache stops at 8 ms at the limit of the porous zone. The gas at the front of the panache deviates sideways and a large whirlpool forms above the baffle. The speed reaches 40 m/s in the panache. The whirlpool sucks water from the top and the side of the mock-up. A second smaller whirlpool arises in the central zone as part of the gas cannot cross the free opening.

Two opposite flows superimpose at the top of the mock-up: argon moves outwards whereas water is pulled inwards by the large whirlpool. The fluid in the top right corner exerts a major thrust, and therefore the flows progress downwards in the channel. The flows reverse in the CCP, and slow down in the bottom and lateral zones.

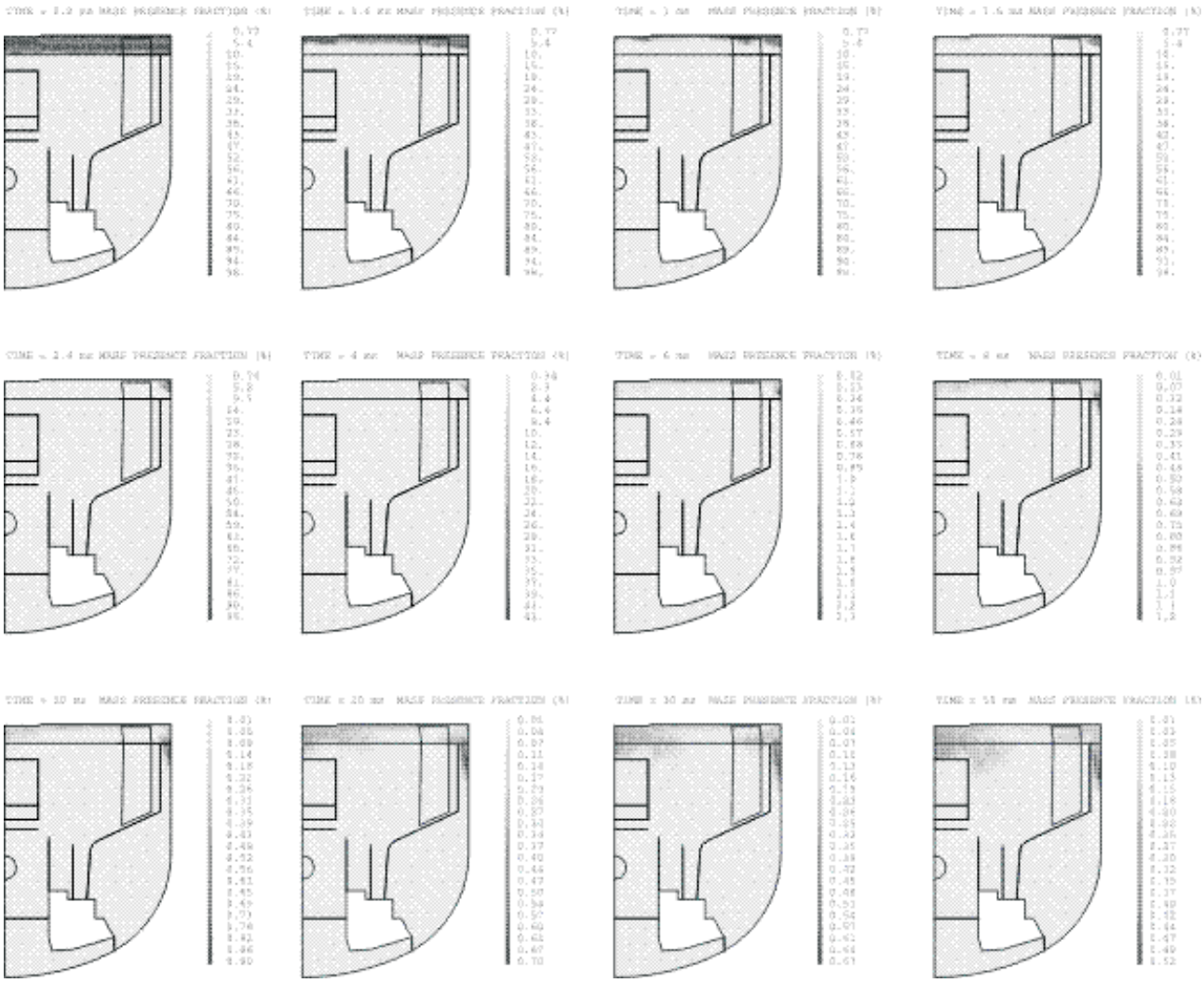

Fig. 10: Mass presence fraction of argon

Between 14 and 20 ms, the whirlpool turns away independently from the rest of the fluid. Not only does it prevent the exit of gas out of the central zone, but it pushes fluid down into this confined area. As a consequence, the impact against the diagrid and the in-pile shell accelerates down the water below the diagrid, and up the water in the CCP.

The whirlpool draws water from the top closure and the top of the CCP, and pushes it in the intermediate zone. The argon bag in the channel is sucked inwards and passes over the top of the internal vessel. On the contrary, argon concentrates at the top of the CCP near the symmetry axis.

After 20 ms, the whirlpool dilutes progressively with the surrounding water, so that it fills half the upper zone at 50 ms. The second small whirlpool continues to twirl in the central area. The argon expands both inwards and downwards. The flows globally slow down in the entire mock-up.

The differences when the computation is done without peripheral structures appear at 5 ms. The horizontal thrust in the channel against the top of the main vessel starts at 5 ms in the new simulation instead of 6 ms. The same advance of 1 ms is also noted at the time of the formation of the main whirlpool. The horizontal argon flows are also more marked. The presence of the porous zone acts as an obstacle, and deviates the water flows upwards towards the top closure. Consequently, the fluid is pushed sooner and somewhat more violently sideways along the top closure.

5.4 Deformed shape

Figs. 13 to 16 present the deformed shapes of the mesh and structures, and the radial and vertical displacements of the structures, respectively. The first structures to deform are those closest to the explosive charge, because they are the first to be impacted by the shock wave.

Almost immediately, the internal shells and the base of the main vessel bend and move away. The bending of the neutron shielding induces a lowering of the shell. The plates of the CCP bend while the bottom of the cylinders buckles, because of the violent flows crossing the free opening.

At 0.6 ms, the upper part of the internal vessel and the lateral wall of the main vessel are pushed outwards by the perpendicular water flows. The bending and the lift of the spacer plates pull the external cylinder of the CCP locally inwards.

Between 0.8 and 2 ms, the top of the neutron shielding opens completely. The bending of the baffle and the lower part of the internal vessel propagates from the bottom to

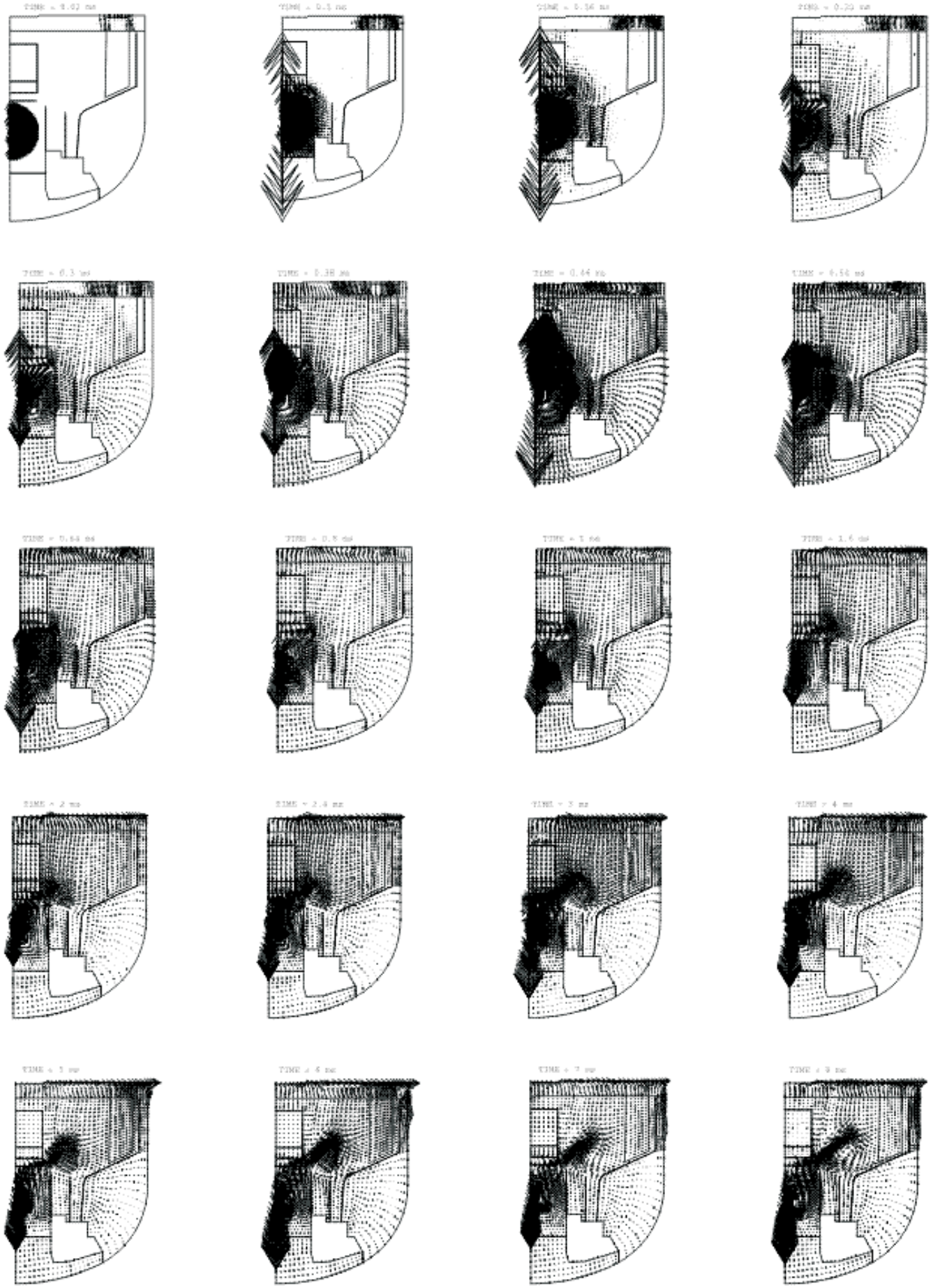

Fig. 11: Fluid flows

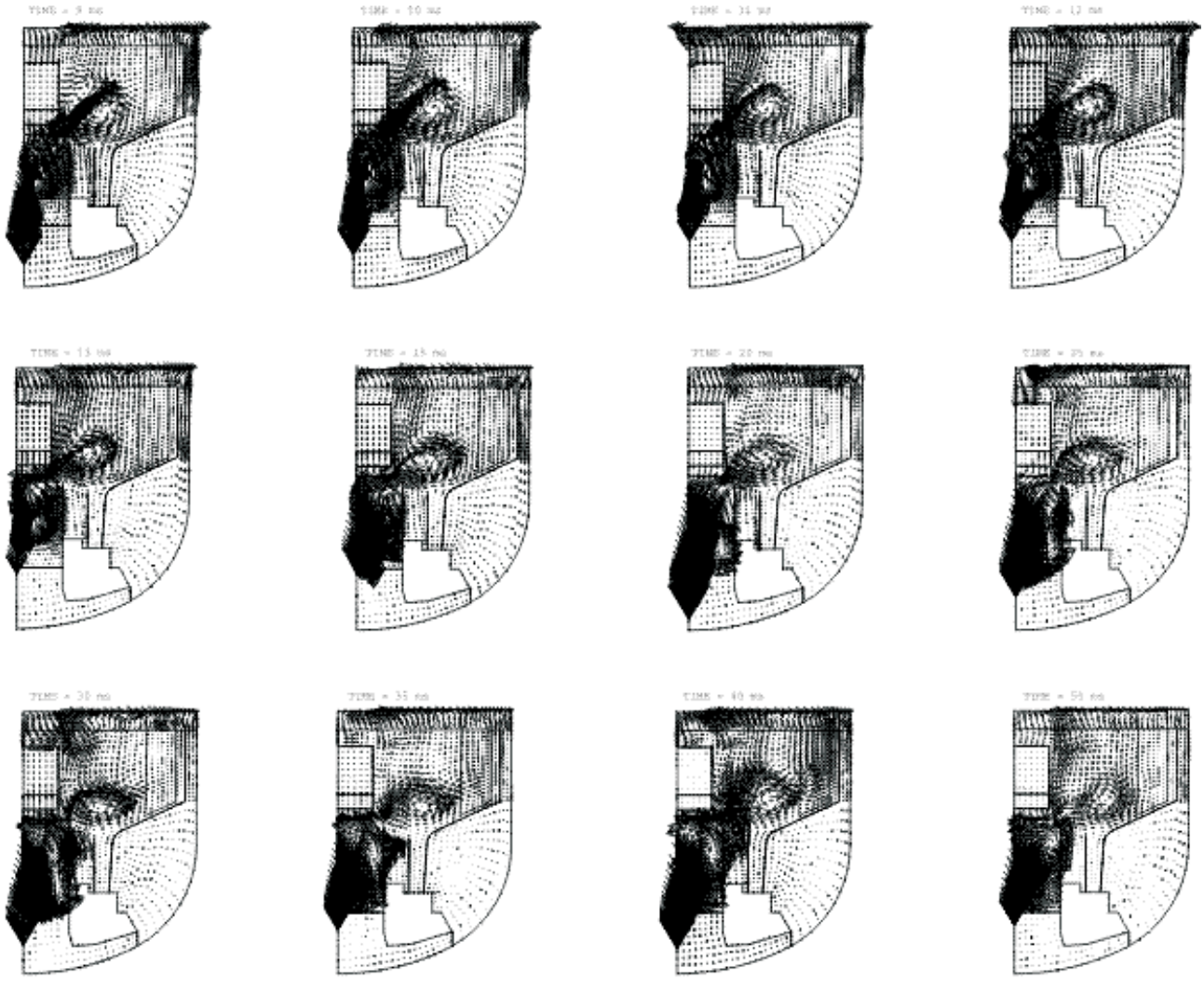

Fig. 11: Fluid flows (following subfigures)

mid-height. The in-pile shell deforms both at the edge and in the centre.

The entire main vessel lowers owing to the high thrust of the water on its base. As the top of the vessel is blocked, the lowering is proportional to the distance from the top. This lowering pulls down the collar, the CSS, and all the structures attached to the vessel. The only exception concerns the baffle, which becomes rounded and stretched by the top water flows.

A bulge forms at the bottom of the lateral wall of the main vessel and the upper part of the internal vessel. The rigid CSS stays fixed radially. The massive top closure is lifted from 1.5 ms by the impact of the upward-directed water; the lift induces a rotation around the hanging device.

The CCP goes on being lifted. The external cylinder buckles just under the top-closure level. As the heat-insulation lower plate is more rigid than the external cylinder, the splash of water against the heat-insulation induces a bending of the cylinder rather than one of the heat-insulation. The shortening caused by the buckling of the external cylinder contributes to the lift of the CCP plates.

At 2 ms, maximum radial displacements are reached:

- 60 mm at the top of the neutron shielding.
- 45 mm at mid-height of the baffle.
- 25 mm at mid-height of the lower part of the internal vessel.
- 15 mm in the main vessel just below the channel.

At 2.8 ms, the lowering becomes maximum in the centre of the diagrid (–30 mm), at the top of the radial shielding (–30 mm), and at the junction of the lower and intermediate parts of the internal vessel (–20 mm). The CSS lowering is around –10 mm. The very flexible baffle continues to be stretched and lifted because of the fluid rebound against the CSS.

From 3 to 5 ms, globally, the deformation of structures in the lower part of the mock-up remain relatively constant whereas the structures in the upper part suffer large increasing deformations.

The panache of gas flowing out of the central zone and the wide opening of the radial shielding tilt more the top of the

Fig. 12: Fluid speed

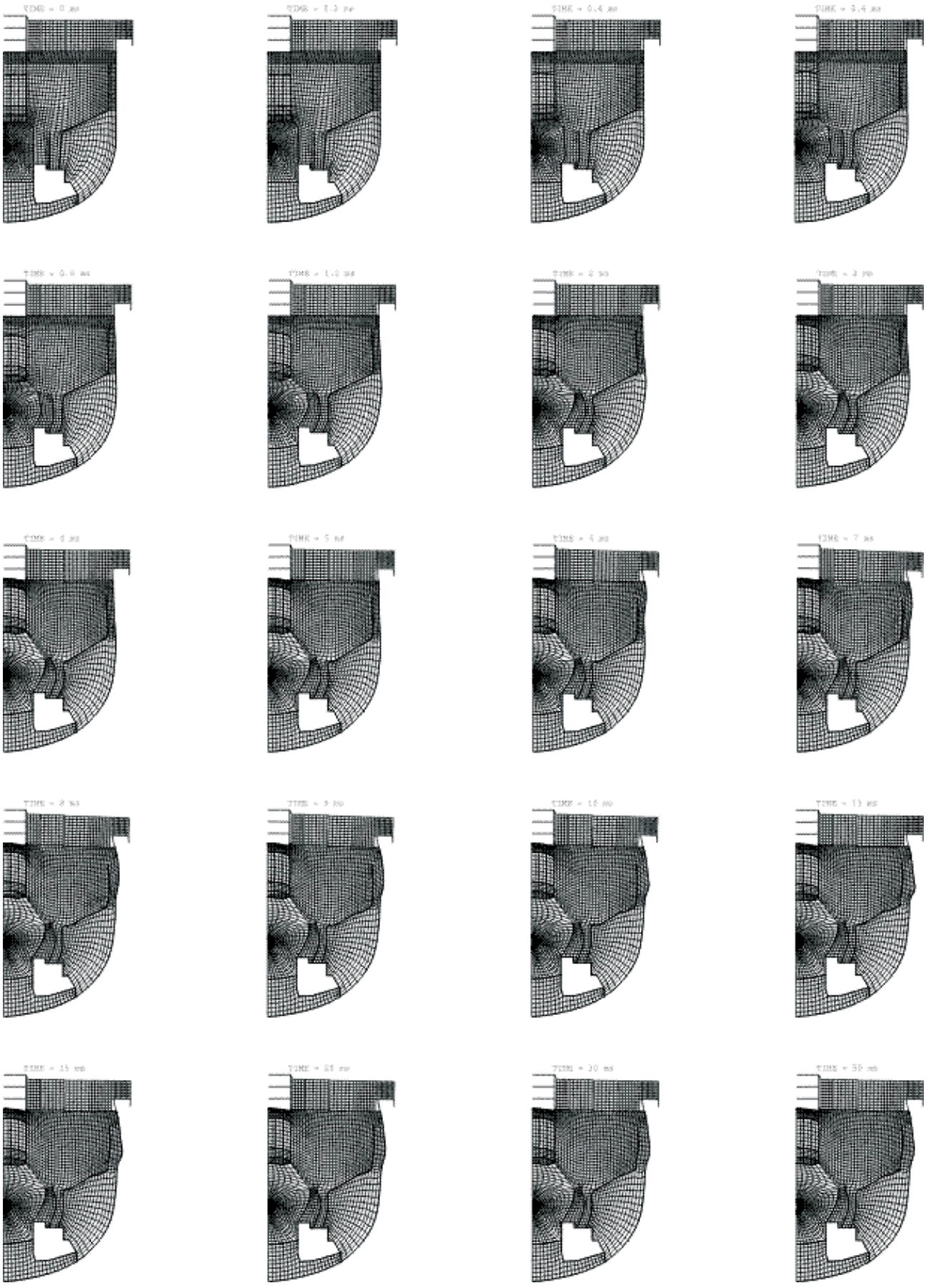

Fig. 13: Deformed shape of the mesh

Fig. 14: Deformed shape of structures

Fig. 15: Radial structure displacements

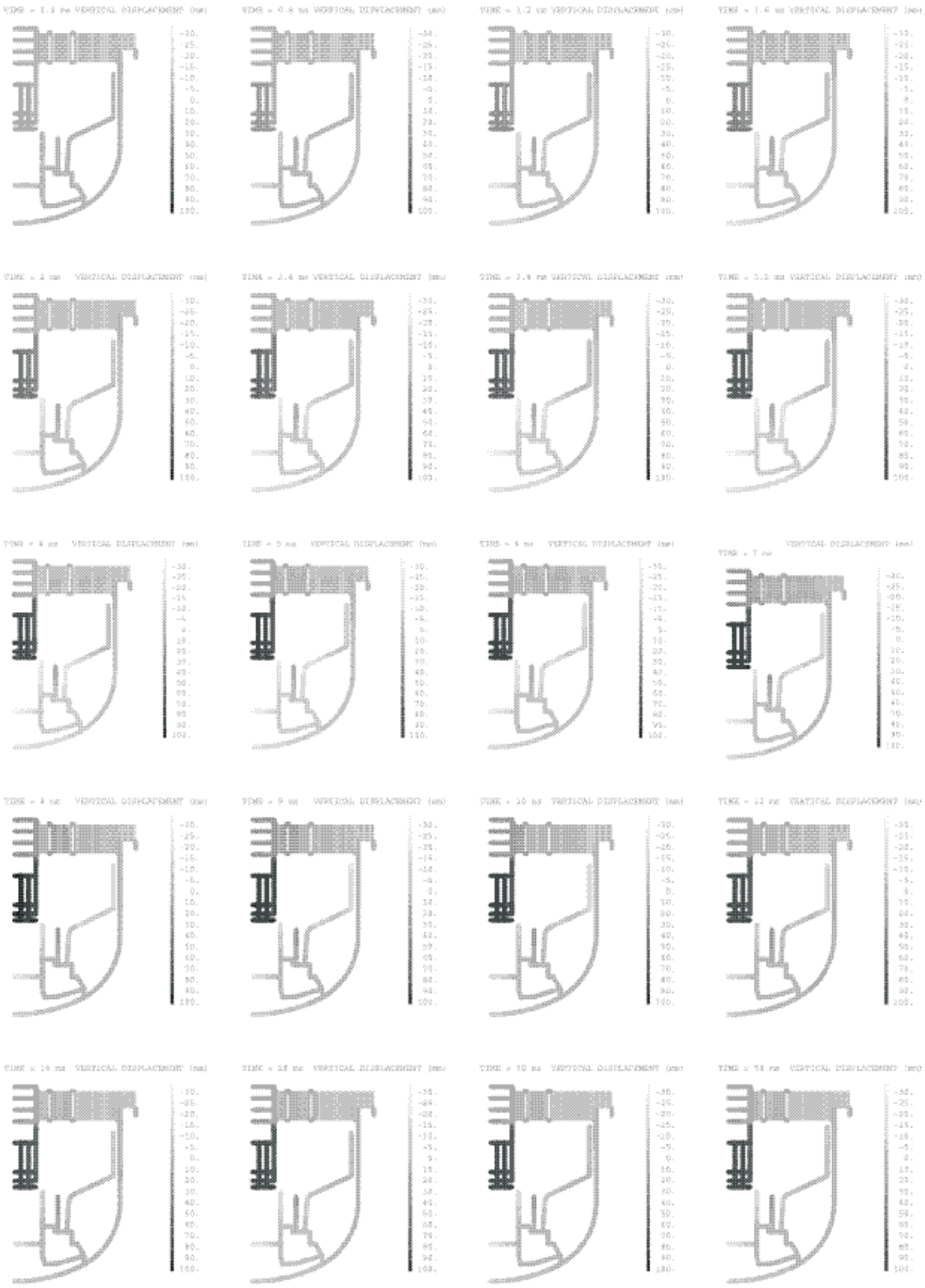

Fig. 16: Vertical structure displacements

baffle, while the downwards flows in the intermediare zone accentuate the bending of the baffle at mid-height. The water hurled by the panache deforms the intermediate and upper parts of the internal vessel, as well as the top of the peripheral components. The upper part of the main vessel bends and moves back upwards.

The CCP continues to be lifted. The upper bulge in the external cylinder crashes against the top closure and the heat-insulation lower plate is lifted and bends at 3.6 ms. The lift of the CCP pulls up the massive structures of the top closure. The joining rings being much more flexible than the massive structures, the pieces shift up mainly at the ring level, and a deformation in stairs appears clearly.

Between 5 and 9 ms, the top of the baffle opens due to the fluid rebounds against the CSS. The main vessel bottom and the diagrid stop lowering and move back up due to the reversal of flows. This lift pulls up the rest of the main vessel, the collar and all the shells attached to the CSS.

The lower and intermediate parts of the internal vessel are pushed back inwards, by water flows rebounding against the rounded corner of the main vessel. The upper part bends and buckles due to the flows against and over the shell. The shell lowers and reaches a maximum opening of 15 mm at 7 ms. The peripheral components – modeled by the porous area – bend at mid-height.

The downward flows of water and pressurised argon in the channel deform the top of the main vessel from 6 ms. The formation of this upper bulge extends the rubber-ring band joining the base of the roof to the main vessel. Progressively, the upper bulge moves down, extends and joins the lower bulge at 9 ms.

In the top closure, the plugs keep their original shape whereas the joining rings are completely out of shape. The maximum displacement reaches 30 mm in the lower heat-insulation plate at 9 ms, and about 20 mm in the small rotating plug.

The rotation around the bottom extremity of the hanging device pulls inwards the entire top closure. The roof slab deforms at the level of the two pieces of different thickness: the thicker piece rotates and moves more than the thinner one, as the latter is tied up to the hanging device.

The CCP continues to be lifted. The external cylinder is partially crashed against the top closure. The in-pile shell, the internal cylinder and the central part of the spacer plates reach a maximum displacement of 100 mm at 9 ms.

As the fluid flows change direction and orient downwards in the CCP, the lower spacer plate and the in-pile shell come closer in the centre and at the edge. The radial displacements at the extremities of the spacer plates and in the main vessel above the collar connection remain constant until the end of the computation.

Between 9 and 12 ms, the main vessel and the structures attached to the CSS keep on moving back upwards. The top of the baffle deforms more or less like rubber, and its radial deformation becomes maximum at 12 ms and reaches 25 mm.

The intermediate part of the internal vessel bends, under the effect of the whirlpool formation. Both the intermediate and upper parts are lifted by the upward flows below the vessel. The flows in the channel push the upper part back inwards. The upper bulge of the main vessel takes a pointed shape, and reaches a maximum radial displacement of 35 mm at 12 ms. The formation of this bulge pulls up the part of the main vessel below.

The top closure and the hanging device rotate back and return after the fluid rebound. The CCP also moves back down, and the spacer plates move aside as the fluid flows reverse.

From 13 to 17 ms, the diagrid moves down again, the edge of the in-pile shell edge moves up, the baffle and the upper part of the internal vessel move back inwards, as the whirlpool pushes the fluid violently inside the central area.

The impact against the diagrid accelerates the water in the bottom zone, and the main vessel bottom lowers again, which pulls down the rest of the main vessel and the structure set attached to it. The top closure rotates again and the entire CCP is lifted once again.

From 25 ms onwards, the structures oscillate around their deformed position according to the evolution of the flows.

Compared with the computation without the peripheral structures, the main differences concern the deformation of the two vessels. The formation of the upper bulge in the main vessel starts sooner at 5 ms in the new simulation. The upper and intermediate parts of the internal vessel deform more:

- The base of the upper part rounds more at 2 ms.
- The top of the internal vessel slightly opens at 7 ms.
- The bending of the intermediate part from 10 ms is really more marked, and leads to a deformation of the porous zone.

5.5 Von Mises stresses in structures

Fig. 17 shows the stresses in both the external and internal structures. Stresses appear first in the central structures and the CCP, due to the impact of the pressure wave. Between 0.2 and 0.3 ms, stresses also appear in the baffle, the two vessels, and the ring joining the CCP to the top of the small rotating plug.

From 0.4 to 0.5 ms, the stress level increases in the structures previously cited, and the ring joining the two rotating plugs. High-stress spots appear at the collar attachment and the thickness change between the rounded and cylindrical parts of the main vessel. There is no stress increase in the CSS as it is supposed rigid.

In the CCP, stresses rise at the plate-cylinder junctions because the fluid lifts and bends the plates. However stresses decrease in the cylinders as they are not coupled to structures. The stress level remains very low in the diagrid support because the constitutive law presents a very low plastic threshold.

From 0.6 to 1.2 ms, stresses decrease in the CCP and the lateral wall of the main vessel. However they increase in:

- The neutron shielding and the baffle because of the formation of the bubble panache.
- The main vessel bottom with a maximum of 650 MPa at 1.2 ms on the symmetry axis.
- The joining rings of the top closure and the hanging device due to the lift and rotation of the top closure.

From 1.2 to 2 ms, the stressed areas of the main vessel base shift towards the collar, and then evolve according to the fluid

Fig. 17: Von Mises stresses

flows. Stresses reach a maximum of 650 MPa at the top of the neutron shielding at 2 ms. They rise in the intermediate part of the internal vessel, but decrease in the lower and upper parts. Even if stresses globally reduce in the CCP, high-stress spots reach 750 MPa at 1.6 ms at the junctions of the spacer plates with the external cylinder.

At 2 ms, stresses reach 250 MPa in the lower heat-insulation plate, 450 MPa where the external cylinder buckles, 500 MPa and 800 MPa in the joining rings between the rotating plugs and between the large plug and the roof. Stresses also increase in the hanging device and the rubber band joining the roof to the main vessel. All these stress rises are due to the lift and the rotation of the top closure.

Between 3 and 5 ms, stresses reduce in the neutron shielding and the in-pile shell, as the inter-shell interval available for fluid flows becomes maximum. They reduce in the lower part of the internal vessel, and rise in the intermediate and upper parts. Stresses reach a maximum of 550 MPa at 3 ms in the baffle, when the panache hits the top head-on.

In the main vessel bottom, the level and the location of stresses are linked to the fluid rebounds. When the fluid impacts the collar at 3 ms, stresses reach 900 MPa in the collar vicinity, and 500 MPa in the rounded corner.

Stresses rise later in the lateral wall and the rubber band joining the roof to the main vessel, when the fluid starts flowing down in the channel. They also increase in the three upper rings.

From 6 to 17 ms, stresses globally decrease from the bottom to mid-height of the main vessel, and alternate more or less high values at the collar attachment according to the rebounds of the water. Stresses still reach 550 MPa at the level of the upper bulge. The stresses observed at mid-height of the neutron shielding are caused by the thrust of the small whirlpool in the central zone.

As the large whirlpool attracts the fluid from the internal vessel towards the baffle, stresses decrease in the internal vessel, but reach 550 MPa in the baffle at 6 ms. Then the stress level oscillates according to the fluid rebounds against the CSS.

In the CCP, stresses remain very low in the internal and intermediate cylinders because these cylinders are not coupled to the fluid. The in-pile shell and the spacer plates remain submitted to the thrust of the small whirlpool. The stress level at the junctions of the plates with the external cylinder depends on the orientation of the flows inside the plug and the pressure exerted by the large whirlpool.

Stresses increase in the joining rings and the hanging device between 6 and 10 ms simultaneously with the lift in stairs of the top closure. The highest stresses (900 MPa) are observed at 12 ms in the ring between the roof and the large rotating plug. Then stresses decrease as the water flows back downwards.

From 20 to 50 ms, stresses decrease in the lower part of the mock-up. However, a high-stress spot persists at 20 and 35 ms at the collar attachment and at the level of the upper bulge in the main vessel.

At the top of the mock-up and particularly in the rings, stresses evolve according to the flow orientation in the upper zone. The CCP presents high-stress points up to 900 MPa at 25 ms at the junctions of the plates with the external cylinder, when the large whirlpool massively sucks down fluid from the top closure along the CCP.

The stress level remains very low in the rigid structures (massive pieces of the top closure, CSS). In the diagrid support, stresses remain limited as the shell becomes almost immediately plastic and suffers large deformations compared to the stress level.

Compared with the computation without the peripheral structures, stresses are higher until the formation of the main whirlpool and lower afterwards. They are higher:

- In the intermediate part of the internal vessel from 0.4 ms, in the entire internal vessel and the rotating plug-roof ring from 3 to 6 ms, since the fluid tends to flow around the porous zone.
- At the bottom of the main vessel between 0.8 and 3 ms as if the fluid thrust were slightly higher with the porous model.
- In the lateral wall of the main vessel between 4 and 6 ms due to the sooner formation of the upper bulge.

Stresses are slightly lower from 8 ms in the CCP with the porous simulation. Between 10 and 25 ms, the maximum stresses in the top closure occur at different times in the two simulations.

5.6 Plastic strains in structures

Fig. 18 shows the plastic strains in structures versus time. Due to the impact of the shock wave, the entire neutron shielding suffers plastic deformations from 0.2 ms. At 0.3 ms, the baffle and the edge of the diagrid support become plastic. Small plastic strains appear in the lower part of the CCP.

From 0.4 to 0.8 ms, the lower part of both vessels, and the junction of the spacer plates with the external cylinder become plastic.

Between 1 and 1.2 ms, the plastic level increases strongly in the structures previously cited. Plastic strains appear at the top of the CCP external cylinder, and in the ring joining the two rotating plugs.

The strain level reaches:

- 40 % at 1.6 ms at the top of the neutron shielding.
- 30 % at 2.2 ms at mid-height of the baffle.
- 25 % at 4 ms at the junction of the CCP external cylinder with the heat-insulation plate.
- 12 % at 4 ms in the rings between the rotating plugs and the roof.
- 8 % in the centre of the diagrid support at 1.6 ms, and in the lower part of the internal vessel at 4 ms.
- 6 % in the heat-insulation plate at 5 ms.
- 4 and 5 % at the bottom and at the level of the lower bulge of the main vessel, respectively.

From 6 ms onwards, the plastic strains remain constant in the shielding, the baffle, the diagrid, the main vessel bottom and most of the CCP.

On the contrary, strains increase at the junction of the lower and intermediate parts of the internal vessel, and in the lateral wall of the main vessel (they reach 8 % at 10 ms in the channel during the formation of the upper bulge). Maximum plastic strains of 14 % and 20 % are observed at 14 ms, in the rings between the small and large rotating plugs and between the large plug and the roof slab, respectively.

Fig. 18: Plastic strains

The strain levels in the computations with and without the peripheral structures are globally the same.

6 Conclusion

In this paper, we present a porosity model that enables us to take into account, in a simplified way, the influence of complex structures on a fluid transient flow and an application of this method to the simulation of an explosion.

The method is based on models representing porous media and consists in averaging structures with the surrounding fluid as if the structures were solid pores inside a fluid. It was specifically developed to model fast transient phenomena without phase change, without heat transfers and described with a Eulerian formulation.

The present method was implemented in the EUROPLEXUS computer code to describe some internal structures of a reactor in the case of a Hypothetical Core Disruptive Accident in Liquid Metal Fast Breeder Reactors. However, this method can be adapted to any kind of problem involving a transient phenomenon with a fluid flow going through a structure set of complex shape.

The MARS mock-up is a small-scale replica of a Fast Breeder Reactor. It contains all the internal structures of the reactor block. However, the fluids intervening in the real accident were replaced by water, argon and an explosive charge in the experiment in order to make the test easier to manage.

The mesh includes classical shells or massive structures to represent the external and internal components, as well as a porous medium to describe the internal structures of complex geometry. The internal fluids are described by the specific CDA constitutive law implemented on purpose in the EUROPLEXUS code for computing this kind of explosion.

The main results observed during the simulation of the accident concern the propagation of a shock wave from the centre of the mock-up towards the external structures, which loads and deforms all the structures.

The high-pressure gas bubble in the central part of the mock-up expands in the rest of the mock-up. This expansion contributes to accelerate and hurl the water against all the structures. The argon layer under the top closure is pushed sideways in the top right-hand corner and flows partially into the channel between the internal and main vessels.

The structures most in demand are the neutron shielding and the core cover plug because of their proximity to the explosive charge. The neutron shielding opens like a flower, the Core Cover Plug is lifted and partially buckles. The main vessel lowers at the bottom and bends twice in the lateral wall, thus forming two bulges. The top closure deforms in stairs due to the weak rigidity of the joining rings linking the massive slabs (plugs and roof).

The development of the porous model with the application to the simulation of the Core Disruptive Accident in the MARS mock-up brings to an end a series of numerical simulations performed since the 1980s on the MARA 8, MARA 10 and MARS mock-ups to improve the understanding of this kind of accident and to validate the CDA models implemented in the EUROPLEXUS code.

References

[1] Louvet, J.: Containment Response to a Core Energy Release. Main Experimental and Theorical Issues – Future Trends. In: *Proc. 10th Int. Conf. on Structural Mechanics in Reactor Technology*, Vol. E, Anaheim (USA), August 1989, p. 305–310.

[2] Bour, C., Spérandio, M., Louvet, J., Rieg, C.: LMFBR's Core Disruptive Accident. Mechanical Study of the Reactor Block. In: *Proc. 10th Int. Conf. on Structural Mechanics in Reactor Technology*, Vol. E, Anaheim (USA), August 1989, p. 281–287.

[3] Acker, D., Benuzzi, A., Yerkess, A., Louvet, J.: MARA 01/02 – Experimental Validation of the SEURBNUK and SIRIUS Containment Codes. In: *Proceeding 6th Int. Conf. on Structural Mechanics in Reactor Technology*, Paris (France), August 1981, paper E 3/6.

[4] Smith, B. L., Fiche, C., Louvet, J., Zucchini, A.: A Code Comparison Exercise Based on the LMFBR Containment Experiment MARA 04. In: *Proc. 8th Int. Conf. on Structural Mechanics in Reactor Technology*, Brussels (Belgium), August 1985, paper E 4/7, p. 151–157.

[5] Fiche, C., Louvet, J., Smith, B. L., Zucchini, A.: Theoretical Experimental Study of Flexible Roof Effects in an HCDA's Simulation. In: *Proc. 8th Int. Conf. on Structural Mechanics In Reactor Technology*, Brussels (Belgium), August 1985, paper E 4/5, p. 139–144.

[6] Louvet, J., Hamon, P., Smith, B. L., Zucchini, A.: MARA 10: an Integral Model Experiment in Support of LMFBR Containment Analysis. In: *Proc. 9th Int. Conf. on Structural Mechanics in Reactor Technology*, Vol. E, Lausanne (Switzerland), August 1987, p. 331–337.

[7] Falgayrettes, M., Fiche, C., Granet, P., Hamon, P., Barrau, P., Magnon, B., Jalouneix, J., Nédélec, M.: Response of a 1/20 Scale Mock-Up of the Superphenix Breeder Reactor to an HCDA Loading Simulation. In: *Proc. 7th Int. Conf. on Structural Mechanics in Reactor Technology*, Chicago (USA), 1983, paper E 4/1, p. 157–166.

[8] Lepareux, M., Bung, H., Combescure, A., Aguilar, J.: Analysis of a CDA in a LMFBR with a Multiphasic and Multicomponent Behaviour Law. In: *Proc. 11th Int. Conf. on Structural Mechanics in Reactor Integrity*, Tokyo (Japan), August 1991, paper E 13/1, p. 371–376.

[9] Casadei, F., Daneri, A., Toselli, G.: Use of PLEXUS as a LMFBR Primary Containment Code for the Cont Benchmark Problem. In: *Proc. 10th Int. Conf. on Structural Mechanics in Reactor Technology*, Anaheim, August 1989, paper E 13/1, p. 299–304.

[10] Benuzzi, A.: Comparison of Different LMFBR Primary Containment Codes Applied to a Benchmark Problem. *Nuclear Engineering and Design*, Vol. **100** (1987), p. 239–249.

[11] Lepareux, M., Bung, H., Combescure, A., Aguilar, J., Flobert, J. F.: Analysis of an HCDA in a Fast Reactor With a Multiphase and Multicomponent Behavior Law. In: *Proc. 12th Int. Conf. on Structural Mechanics in Reactor Technology*, Stuttgart (Germany), August 1993, paper E 7/2, p. 197–202.

[12] Cariou, Y., Pirus, J. P., Avallet, C.: LMR Large Accident Analysis Method. In: *Proc. 14th Int. Conf. on Structural*

Mechanics in Reactor Technology, Lyon (France), August 1997, paper P 3/7, p. 395–402.

[13] Cariou, Y., Spérandio, M., Lepareux, M., Christodoulou, K.: LMFBR's Whole Core Accident. Validation of the Plexus Code by Comparison with MARA Tests. In: *Proc. 12th Int. Conf. on Structural Mechanics in Reactor Technology*, Stuttgart (Germany), August 1993, paper E 7/4.

[14] Cariou, Y., Lepareux, M., Noé, H.: LMR's Whole Core Accident. Validation of the Plexus Code by Comparison with MARS Test. In: *Proc. 14th Int. Conf. on Structural Mechanics in Reactor Technology*, Lyon (France), August 1997, paper P 2/6, p. 339–346.

[15] Casadei, F., Halleux, J. P., Huerta, A.: Dynamic Response of Fluid-Structure Systems by PLEXIS-3C. In: *Proc. European Conf. on New Advances in Computational Structural Mechanics*, Giens (France), April 1991.

[16] Robbe, M. F., Lepareux, M., Treille, E., Cariou, Y.: Numerical Simulation of an Explosion in a Simple Scale Model of a Nuclear Reactor. *Journal of Computer Assisted Mechanics and Engineering Sciences*. Vol. **9** (2002), No. 4, p. 489–517.

[17] Robbe, M. F., Lepareux, M., Cariou, Y.: Numerical Interpretation of the MARA 8 Experiment Simulating a Hypothetical Core Disruptive Accident. *Nuclear Engineering and Design*. Vol. 0 (2003), p. 119–158.

[18] Robbe, M. F., Lepareux, M., Treille, E., Cariou, Y.: Numerical Simulation of a Hypothetical Core Disruptive Accident in a Simple Scale Model of a Nuclear Reactor. *Nuclear Engineering and Design*. Vol. **223** (2003), No. 2, p. 159–196.

[19] Robbe, M. F., Casadei, F.: Comparison of Various Models for the Simulation of a Core Disruptive Accident in the MARA 10 Mock-Up. *Nuclear Engineering and Design*. Vol. **232** (2004), p. 301–326.

[20] Robbe, M. F., Lepareux, M., Seinturier, E.: Computation of a Core Disruptive Accident in the MARS Mock-Up. *Nuclear Engineering and Design*. Vol. **235** (2005), p. 1403–1440.

[21] Robbe, M. F., Bliard, F.: A Porosity Method to Describe the Influence of Internal Structures on a Fluid Flow in Case of Fast Dynamics Problems. *Nuclear Engineering and Design*. Vol. **215** (2002), p. 217–242.

[22] Robbe, M. F., Lepareux, M.: Representation of Complex 3d-Structures by a Porosity Method - Application to the Simulation of an Explosion. In: *Proc. European Nuclear Conference*, Versailles (France), December 2005.

[23] Butterworth, D.: The Development of a Model for Three-Dimensional Flow in Tube Bundles. *Int. Journal of Heat and Mass Transfer*. Vol. **1** (1978), p. 253–256.

[24] NERSA: The Creys-Malville Power Plant. Electricité de France, Direction de l'équipement, Région d'équipement Alpes-Lyon (France), 1987.

[25] David, F.: Etude d'une composition explosive flegmatisée. Applications la déformation d'une cuve. In: *Proc. Symposium sur les hautes pressions dynamiques*, Paris (France), 1978.

[26] Lepareux, M., Hoffmann, A., Schwab, B., Bung, H.: Plexus – A General Computer Program for Fast Dynamic Analysis. In: *Proc. Conference on Structural Analysis and Design on Nuclear Power Plant*, Porto Alegre (Brazil), 1984.

[27] Robbe, M. F., Lepareux, M., Bung, H.: Plexus – Notice théorique. *CEA report* DMT/94-490, 1994.

[28] Casadei, F., Halleux, J. P.: Europlexus: A Numerical Tool for Fast Transient Dynamics with Fluid-Structure Interaction. In: *Proc. SAMTECH users' conference*, Toulouse (France), February 2003.

[29] Robbe, M. F., Dolensky, B., Strub, C., Galon, P.: Overview of German and French works Relative to Slug Impact – Numerical Results. *Bulgarian Journal of Theoretical and Applied Mechanics*. Vol. **36** (2006), No. 1.

[30] Robbe, M. F., Vivien, N., Valette, M., Berglas, E.: Use of Thermalhydraulic and Mechanical Linked Computations to Estimate the Mechanical Consequences of a Steam Explosion. *Journal of Mechanical Engineering*. Vol. **52** (2001), No. 2, p. 65–90.

[31] Robbe, M. F., Lepareux, M.: Evaluation of the Mechanical Consequences of a Steam Explosion in a Nuclear Reactor. *Bulgarian Journal of Theoretical and Applied Mechanics*. Vol. **32** (2002), No. 1, p. 48–84.

[32] Robbe, M. F., Sardain, P.: Comparison of Several Simplified Models and Scenarios to Simulate a Steam Explosion in a Tank. *Journal of Mechanical Engineering*. Vol. **54** (2003), No. 2, p. 82–100.

[33] Lepareux, M., Schwab, B., Hoffmann, A., Jamet, P., Bung, H.: Un programme général pour l'analyse dynamique rapide – Cas des tuyauteries. In: *Proc. Colloque Tendances Actuelles en Calcul des Structures*, Bastia (France), 1985.

[34] Lepareux, M., Schwab, B., Bung, H.: Plexus: A General Computer Program for the Fast Dynamic Analysis. The Case of Pipe-Circuits. In: *Proc. 8th Int. Conf. on Structural Mechanics in Reactor Technology*, Brussels (Belgium), 1985, paper F1 2/1.

[35] Robbe, M. F., Potapov, S.: Modeling of the Depressurisation Induced by a Pipe-Rupture in the Primary Circuit of a Nuclear Plant. *Revue Européenne des Eléments Finis*. Vol. **12** (2003), No. 4, p. 459–485.

[36] Potapov, S., Bliard, F., Tephany, F.: Simulation de la décompression du réacteur HDR avec le code de dynamique rapide EUROPLEXUS. *Revue Européenne des Eléments Finis*. Vol. **11** (2002), No. 5, p. 667–694.

[37] Potapov, S.: Modelling of Aquitaine II Pipe Whipping Test with Europlexus Fast Dynamic Code. In: *Proc. 17th Int. Conf. on Structural Mechanics in Reactor Technology*, Prague (Czechoslovakia), August 2003, paper 01/5.

[38] Robbe, M. F., Lepareux, M., Trollat, C.: Hydrodynamic Loads on a PWR Primary Circuit Due to a LOCA. *Nuclear Engineering and Design*. Vol. **211** (2002), p. 189–228.

[39] Robbe, M. F., Potapov, S., Teffany, F.: Simulation of the Depressurisation Occurring At The Beginning of a LOCA in a 4-Loop PWR. *Nuclear Engineering and Design*. Vol. **223** (2003), p. 159–196.

[40] Studer, E., Galon, P.: Hydrogen Combustion Loads – Plexus Calculations. *Nuclear Engineering and Design* Vol. **174** (1997), p. 119–134.

[41] Lepareux, M., Michelin, J. M. Thiault, D.: Plexus-R: une extension de Plexus la robotique. *CEA Report* DMT/94-138, 1994.

Dr. Marie-France Robbe
phone: 331 69088749
e-mail: sdufour@free.fr

38 Rue de Migneaux
91300 Massy, France